Atmospheric Environment 231 (2020) 117563

Contents lists available at ScienceDirect

Atmospheric Environment

journal homepage: http://www.elsevier.com/locate/atmosenv

Source and formation of fine particulate nitrate in South China: Constrained by isotopic modeling and online trace gas analysis

Tao Su [a,d], Jun Li [a,*], Chongguo Tian [b], Zheng Zong [b], Duohong Chen [c,**], Gan Zhang [a]

[a] State Key Laboratory of Organic Geochemistry and Guangdong Key Laboratory of Environmental Protection and Resources Utilization, Guangzhou Institute of Geochemistry, Chinese Academy of Sciences, Guangzhou, 510640, China
[b] Key Laboratory of Coastal Environmental Processes and Ecological Remediation, Yantai Institute of Coastal Zone Research, Chinese Academy of Sciences, Yantai, 264003, China
[c] Guangdong Environmental Monitoring Center, Guangzhou, 510308, China
[d] University of Chinese Academy of Sciences, Beijing, 100049, China

HIGHLIGHTS

- Characteristics of NO_3^- were studied by analysis of $\delta^{15}N$-$\delta^{18}O$ and trace gas in PRD.
- Both of $\delta^{15}N$–NO_3^- and $\delta^{18}O$–NO_3^- values were low in spring and high in winter.
- ·OH generation was predominant NO_3^- formation from Monte Carlo simulation.
- Coal combustion was the predominant source of NO_3^- modeled by the Bayesian.

ARTICLE INFO

Keywords:
Pearl River Delta
Nitrate
Isotope
Source apportionment

ABSTRACT

NO_x is an important precursor of fine particulate matter ($PM_{2.5}$) and O_3 and its oxidation product NO_3^- may be the main driver of $PM_{2.5}$. In this study, 76 daily fine particle samples were collected from a site in South China, and the characteristics of NO_3^- were studied using an improved Bayesian mixing model based on $\delta^{15}N$–$\delta^{18}O$ compositions and online trace gas analysis. NO_3^- concentrations ranged from 0.60 to 21.7 μg/m^3, accounting for 6.0 ± 3.3% of total $PM_{2.5}$ on average. $\delta^{15}N$–NO_3^- values varied from −3.6 to 15.4‰ (average: 7.5 ± 3.3‰). Driven by changes in chemical pathways and environmental parameters, including equilibrium fractionation and thermodynamic effects, $\delta^{15}N$–NO_3^- values were lowest in spring and highest in winter. $\delta^{18}O$–NO_3^- values varied from 21.0 to 90.1‰ (average: 62.4 ± 14.0‰). In spring, the lowest $\delta^{18}O$–NO_3^- values were observed due to high proportions originating from $\cdot HO_2$ and ·OH reaction pathways, as well as changes in other parameters. In winter, the highest $\delta^{18}O$–NO_3^- values were observed due to cold and dry weather, along with the lowest proportion from the ·OH pathway. Moreover, the trace gases CO, O_3, NO_x, SO_2, and N_2O_5 were measured seasonally to determine the main drivers of seasonality in $\delta^{15}N$–$\delta^{18}O$ composition. Monte Carlo simulation was used to estimate the relative contributions of the gas-phase reactions of NO_2 and ·OH radicals and the hydrolysis of N_2O_5. The results showed that the ·OH generation pathway was predominant throughout the year, with relative contributions of 72 ± 18%, 76 ± 16%, 63 ± 17% and 39 ± 15% in spring, summer, fall and winter, respectively. Coal combustion (50.1 ± 13.8%) was the predominant source of NO_3^- identified using the Bayesian model, and originated from central and southern Guangdong Province, as indicated by potential source contribution function analysis.

1. Introduction

Rapid economic and industrial development in China have resulted in frequent heavy haze pollution events that have caused public alarm and official concern due to their significant adverse effects on the environment, human health, and climate (Cao, 2014). To address this problem, the 'Air Pollution Prevention and Control Action Plan (2013-17)' was introduced to control major harmful pollutants during

* Corresponding author.
** Corresponding author.
E-mail addresses: junli@gigi.ac.cn (J. Li), chenduohong@139.com (D. Chen).

https://doi.org/10.1016/j.atmosenv.2020.117563
Received 20 January 2020; Received in revised form 20 April 2020; Accepted 23 April 2020
Available online 27 April 2020

heavy pollution events (Sheehan et al., 2014). According to the Bulletin on China's Environmental Situation 2014–2017 (Fig. S1), three major air pollutants showed slightly different dynamics in typical cities in China after implementation of the plan. These changes included steady decreases of fine particulate matter ($PM_{2.5}$) and SO_2 levels but without marked decreases of NO_x levels, except in Guangzhou and Shanghai (decreases of 10.6% and −0.411%, respectively). NO_x is the precursor of NO_3^-. As a result, NO_3^- concentrations were higher in aerosols than in sulfate in some regions. These observations indicate that control of NO_x pollution in China requires further attention.

To effectively control NO_x emissions, it is necessary to determine the chemical conversion processes of NO_x and to identify and quantify NO_x sources. Generally, NO_x forms particulate NO_3^- through the gas-phase reaction of ·OH and NO_2 or hydrolysis of N_2O_5 (Text S1). Heterogeneous reactions of N_2O_5 may involve O_3, NO_2, and NO_3. Under the high-O_3 conditions of the urban atmosphere in China, the contribution of NO_3^- formed via N_2O_5 hydrolysis to haze is important. For example, based on 2 years of online measurement of O_3 levels, N_2O_5 hydrolysis is considered the primary formation pathway of fine particulate NO_3^- during haze events in the western Yangtze River Delta (YRD) region (Sun et al., 2018). Furthermore, N_2O_5 and $ClNO_2$ in South China were measured online via mass spectrometry, and N_2O_5 heterogeneous reactions were a significant source of aerosol NO_3^- on hazy days (Yun et al., 2018). The origins of NO_x are complex, because it has both natural and anthropogenic sources. Source apportionment of NO_x has been based on air quality models, such as the Comprehensive Air Quality Model (CAMx) and Community Multiscale Air Quality (CMAQ) model (Han et al., 2009; Zhao et al., 2013). However, these source apportionment models usually include some level of uncertainty, which may lead to large differences in magnitude (Shimadera et al., 2015).

Based on the nitrogen and oxygen stable isotopic composition ($\delta^{15}N$–NO_3^- and $\delta^{18}O$–NO_3^-) of NO_3^- in particulate matter, the source and oxidation pathway of NO_x may be revealed (Fang et al., 2011; Zong et al., 2017). Despite a large range of end-member values for $\delta^{15}N$-NO_x (Felix and Elliott, 2014) and fractionation effects that occur during the transport and transformation of atmospheric NO_3^-, nitrogen stable isotopic composition has been used to reflect NO_x sources in previous studies (Fang et al., 2011; Felix and Elliott, 2014; Zong et al., 2017). Furthermore, the sources of NO_x in North China have been quantitatively apportioned using nitrogen isotopic composition ($\delta^{15}N$–NO_3^-) linked with a Bayesian mixing model, revealing that biomass burning, coal combustion, mobile sources, and biogenic soil emissions contribute 27.78 ± 8.89%, 36.53 ± 6.66%, 22.01 ± 6.92%, and 13.68 ± 3.16%, respectively, of total NO_x (Zong et al., 2017). Oxygen isotope ($\delta^{18}O$–NO_3^-) analysis of NO_3^- can also play a role in tracing its generation pathways. Due to the rapid exchange of oxygen atoms between NO_x and oxidants, the $\delta^{18}O$–NO_3^- value is determined from its generation pathways (Text S1), rather than the original NO_x sources (Hastings et al., 2003). The $\delta^{18}O$ value of O_3 (90–122‰) differs markedly from that of water (−25–0‰) (Fang et al., 2011). Therefore, the respective contributions of the gaseous oxidation and hydrolysis generation pathways can be assessed using a Monte Carlo simulation based on $\delta^{18}O$–NO_3^- values in aerosols (Zong et al., 2017).

The Pearl River Delta (PRD) in South China is one of the most industrialized and densely populated regions of China, with a land area of 42,200 km^2 and a population of 57.2 million. The PRD is one of three major pollution control regions addressed in the 'Air Pollution Prevention and Control Action Plan (2013-17)', issued by the State Council on September 10, 2013 (Sheehan et al., 2014). Additionally, the PRD region is a major area of NO_x pollution based on the average satellite-derived NO_x emission inventory for China (Fig. S2). The MIX inventory was developed to estimate NO_x emissions data for Guangdong Province in 2010, and the results showed that the main contributors were the power (37.7%), industry (31.8%), and residential (28.3%) sectors (Li et al., 2017). Using the CAMx modeling system and O_3 source apportionment technology (OSAT), heavy-duty diesel vehicles and industrial point sources were identified as the two main local sources of ground-level NO_x in the PRD in 2011 (Lu et al., 2016). These results differ greatly, further illustrating the necessity of employing new methods to apportion the major sources of NO_x in the PRD region (Tao et al., 2018). In previous studies, the nitrogen isotopic composition of NO_3^- in precipitation samples collected in Guangzhou has been used to reveal possible sources of NO_x, which qualitatively supported the importance of anthropogenic contributions, particularly from coal combustion (Fang et al., 2011; Jia and Chen, 2010). Although the importance of N_2O_5 hydrolysis to NO_3^- formation has been confirmed during hazy days in southern China using online measurement via mass spectrometry (Yun et al., 2018), the annual variations in the contribution of N_2O_5 hydrolysis to particulate NO_3^- formation remain unknown. In addition, other oxidation pathways are important under the conditions of high temperature (T) and humidity found in the PRD region (Lu et al., 2014; Ma et al., 2017). Based on oxygen ($\delta^{18}O$–NO_3^-) isotope values below the expected minimum of +55‰ in precipitation, the reaction of NO with peroxy radicals has been proposed (Fang et al., 2011).

In this study, the nitrogen ($\delta^{15}N$–NO_3^-) and oxygen ($\delta^{18}O$–NO_3^-) isotopes of offline particulate NO_3^- were determined, the sources and transformation pathways of NO_x were identified using an improved Bayesian mixing model, and the influencing and controlling factors were revealed by combining the online meteorological parameters with trace gas data. The results provide actionable information for developing NO_x control strategies in the PRD.

2. Materials and methods

2.1. Sampling

The sampling site is located on a building roof (~10 m height) at the Guangdong atmospheric supersite, a semi-rural site located in Hua Guo Shan (22°42′N, 112°55′E), southwest of the city of Heshan (HS), from August 1, 2013, to November 13, 2014. Details about sampling site can be found in Fig. S3 and a previous report (Yun et al., 2018). A total of 76 samples of $PM_{2.5}$ and three sets of blank samples were collected over a period of 24 h (starting at 08:00 and ending at 08:00 the following day) each week. All $PM_{2.5}$ samples were collected on pre-combusted quartz filters (8 × 10 inch; Pall Corp., Port Washington, NY, USA) using a high-volume sampler equipped with a $PM_{2.5}$ impactor (Xintuo Analytical Instruments, Shanghai, China) at a flow rate of 1 m^3/min. After sampling, the filters were covered with aluminized paper and packed in a sealed bag, which was stored in a refrigerator at −20 °C until chemical analysis. The trace gases CO, O_3, NO_x, and SO_2 were determined online. CO was measured with a gas filter correlation analyzer (model 48i; Thermo Scientific, Waltham, MA, USA). O_3 was detected with an ultraviolet photometric analyzer (model 49i; Thermo Scientific). NO and NO_2 were determined with a chemiluminescence instrument (model 42iTL; Thermo Scientific). SO_2 was observed using a pulsed fluorescence analyzer (model 43iTLE; Thermo Scientific). The seasonal variations of trace gases are presented in Fig. S4. Additionally, the N_2O_5 concentration was calculated using steady-state predictions due to a lack of observation data (Brown et al., 2005) (Text S7). Meteorological parameters were measured with a portable weather station (WXT520; Vaisala, Vantaa, Finland), including wind speed (WS), wind direction (WD), T, relative humidity (RH) and atmospheric pressure (P). Additionally, solar radiation was detected using a pyranometer (CMP22; Kipp & Zonen B.V., Delft, Netherlands). The parameters measured during the sampling period are illustrated in Fig. S5.

2.2. Chemical and isotopic analysis

$PM_{2.5}$ concentrations were calculated as the difference in filter weight before and after sampling. Before and after sampling, the filters were subjected to 24 h equilibration at 25 °C and 50% RH and then weighed gravimetrically using a Sartorius MC5 electronic microbalance.

Organic carbon (OC) and elemental carbon (EC) were analyzed with a carbon analyzer (Sunset Laboratory, Inc., Tigard, OR, USA) based on the National Institute for Occupational Safety and Health (NIOSH870) thermal–optical transmittance protocol (Liu et al., 2014). The minimum detection levels (MDLs) of OC and EC were 1.42 ± 0.2 and 0.03 ± 0.2 μgC/cm^2, respectively. Water-soluble ions (SO_4^{2-}, NH_4^+, K^+, Ca^{2+}, Cl^-, Na^+, Mg^{2+}, and NO_3^-) were measured via ion chromatography (761 compact IC; Metrohm, Herisau, Switzerland), the details of which are provided in Text S2. Field blank values were subtracted from sample concentrations. The MDLs of ions were within the range of 5.0–21.0 ng/mL (Table S1).

The values of $\delta^{15}N$–NO_3^- and $\delta^{18}O$–NO_3^- in particulate NO_2^- were measured using the cadmium reduction method (McIlvin and Altabet, 2005; Xiao et al., 2015). To measure the values of $\delta^{15}N$–NO_3^- and $\delta^{18}O$–NO_3^-, NO_3^- concentrations were diluted to 15 μmol/L in 5 mL of 0.5 M NaCl solution. Then, 0.3 g of cadmium powder was added to the solution, and the pH was adjusted to 9 using 0.1 mL of 1 M imidazole solution. The sample bottles were capped tightly with rubber septa and ultrasonically oscillated for 2 h at 40 °C. After standing for 12 h, 4 mL of solution was removed and added to the headspace of a clean bottle, 0.2 mL of 1 M sodium azide buffer solution (containing 10% acetic acid) was added to the bottle to reduce NO_3^- to N_2O, and the bottle was placed upside down for 30 min. Finally, the solution was made basic with the addition of 0.4 mL of 10 M NaOH to stop the reaction. The values of $\delta^{15}N$–N_2O and $\delta^{18}O$–N_2O were analyzed using an isotope ratio mass spectrometer (MAT253; Thermo Fisher Scientific, Waltham, MA, USA). The $\delta^{15}N$ and $\delta^{18}O$ values were reported relative to standards (air N_2 and VSMOW) (Komatsu et al., 2008) as follows:

$$\delta^{15}N\ (‰) = [(^{15}N/^{14}N)_{sample} / (^{15}N/^{14}N)_{air\ N2} - 1] \times 1000 \quad (1)$$

$$\delta^{18}O\ (‰) = [(^{18}N/^{16}N)_{sample} / (^{18}N/^{16}N)_{VSMOW} - 1] \times 1000 \quad (2)$$

In this study, four international reference materials (IAEA-NO_3^-, USGS32, USGS34, and USGS35) were used to correct for drift, oxygen isotope exchange, and blank effects from the process of converting NO_3^- into N_2O. The average standard deviations from replicate analyses of samples and references were 0.3‰ and 0.6‰ for $\delta^{15}N$–NO_3^- and $\delta^{18}O$–NO_3^-, respectively.

2.3. Improved Bayesian mixing model

The Bayesian mixing model used here employs stable isotopes to estimate the probability distributions of source contributions to a mixture, and has been widely applied for this purpose in ecological studies (Moore and Semmens, 2008). The model uses a sampling/importance resampling (SIR) method to estimate the posterior probability of proportions and is also referred to as MixSIR. MixSIR is available through the GreenBoxes code-sharing network (http://conserver.iugo-cafe.org/). The detailed model framework has been described in a previous study (Moore and Semmens, 2008). However, its estimation of the fractionation of $\delta^{15}N$ in the process of converting NO_x into NO_3^- is poorly documented. Previous studies have incorporated a module for balanced NO and NO_2 fractionation into the model to estimate the fractionation of $\delta^{15}N$ through Monte Carlo simulation, thereby constructing a suitable NO_x source apportionment model (Walters and Michalski, 2015, 2016; Zong et al., 2017). Briefly, the improved model requires inputs of isotope ($\delta^{15}N$ and $\delta^{18}O$), T, and end-member $\delta^{15}N$-NO_x data, and returns probability distributions of the contributions of different NO_x sources using MATLAB (MathWorks, Natick, MA, USA). The details of this calculation were reported previously (Zong et al., 2017). From the total of 76 samples, five had $\delta^{18}O$–NO_3^- values less than 40‰ and were deleted during the Bayesian model run; therefore, 71 samples were applied in the model to obtain the probability contribution distribution of the four main NO_x/NO_3^- sources in this study.

2.4. Hybrid single-particle Lagrangian integrated trajectory (HYSPLIT) and potential source contribution function (PSCF) models

To identify the potential impact of the different source regions on NO_x during the sampling period, the air mass back trajectories were computed using the HYSPLIT model, described in Text S4. Then, 36-h air mass back trajectories with a 6-h interval were modeled at 100 m above ground level, generating a total of 76 trajectories that were grouped into four clusters (Fig. S6). The air masses associated with cluster 1 and cluster 2 are of maritime origin, from the middle of the Pacific Ocean and the South China Sea, respectively, which flow in a general southwest-to-east direction toward the PRD region; these air masses correspond to the regions abbreviated MP and SCS, respectively. The air masses associated with cluster 3 and cluster 4 are of continental origin, flowing through Jiangxi and Fujian provinces in a general northwest-to-northeast direction to reach the PRD region, and correspond to the region abbreviations JX and FJ, respectively.

PSCF analysis is a useful method to obtain a probability field for estimating the regional source strength of pollutants based on the results of the HYSPLIT model (Cheng and Kabela, 2016; Zong et al., 2018). The principle of the PSCF model is described in Text S5. In this study, it was employed to assess the potential source regions of the predominant NO_x source factors obtained from the improved MixSIR model results using the corresponding daily median contribution data. As a result, the 36-h average NO_x concentration and its contributions above the 75th percentile during the sampling period were analyzed in a 0.5° × 0.5° spatial grid from 100 to 130°E and from 0 to 30°N (Fig. S7).

3. Results and discussion

3.1. Characteristics of NO_3^- aerosols

The observed concentrations of $PM_{2.5}$ varied widely, ranging from 19.9 to 164 μg/m^3. During the sampling period, the average value at station HS was 80.4 ± 35.8 μg/m^3, 8 times the level at Nanling Background Station (10.0 μg/m^3) (Zhang et al., 2015), and more than twice the health threshold annual standard for China (35.0 μg/m^3). $PM_{2.5}$ concentrations were always elevated in autumn and winter, and showed seasonal fluctuations (Fig. S5). NO_3^- concentrations ranged from 0.60 to 21.7 μg/m^3 (average: 5.40 ± 4.80 μg/m^3), and accounted for 1–16% of $PM_{2.5}$ by mass. A marked seasonal trend of NO_3^- was observed, with the highest value in fall (21.7 μg/m^3) and the lowest in summer (0.60 μg/m^3) (Fig. S5). NO_3^- concentrations measured during cool seasons (fall and winter, 7.40 ± 5.00 μg/m^3) were 3 times higher than those in warm seasons (spring and summer, 2.50 ± 2.60 μg/m^3) (Table S2). The contribution of NO_3^- to $PM_{2.5}$ was significantly positively correlated with PM loading ($R^2 = 0.31$, $P < 0.01$), and suggested that NO_3^- is a major driver of haze episodes characterized by high $PM_{2.5}$ peaks in the PRD. Spatially, the annual mean NO_2^- concentration in this study was slightly lower than that from a background station in North China (6.30 ± 4.90 μg/m^3) (Zong et al., 2017), and significantly lower than those of major cities in the YRD (Ming et al., 2017). These results show that air quality in the PRD is better than that in North China and the YRD. Compared with a study conducted in Guangzhou in 2003, the present NO_3^- concentrations were lower in winter, but slightly higher or comparable in summer (Cao et al., 2012). Previous research indicated that the NO_3^- concentration in the atmosphere of Guangzhou in the PRD increased from 2010 to 2014 (Tao et al., 2017), which underscores the importance of NO_3^- in the atmosphere of the PRD and the necessity for NO_x control in this region.

The seasonal concentration variations of particulate NO_3^- can be controlled by many factors, such as the air mass transport pattern and boundary layer depth, seasonal variations of pollutant emissions, meteorological parameters, and atmospheric oxidation. To identify the potential impacts of various source regions on NO_x during the sampling period, air mass back trajectories were computed using the HYSPLIT

model. During cool seasons, atmospheric NO_x originates from the northeast through highly nitrogen-polluted continental outflow from the central PRD, and the relatively low boundary layer depth facilitates the accumulation of air pollutants (Li et al., 2006), resulting in high NO_3^- content (Text S10). However, during warm seasons, NO_x originates from clean air masses over the SCS, and the relatively high boundary layer depth facilitates the diffusion of air pollutants, resulting in low NO_3^- content (Lu and Fung, 2016). For example, when NO_3^- concentrations were high and their contribution to $PM_{2.5}$ load was large, the WS was below 2 m/s. Anthropogenic pollutant signals (NH_4^+, EC, K^+, nss-Cl^-, SO_4^{2-}) were significantly higher during cool seasons than warm seasons (Liu et al., 2014; Sun et al., 2018) (Fig. S8). Ambient T and RH, which were significantly negatively correlated with NO_3^- (Table S3), also affect the concentration of atmospheric particulate NO_3^- by altering the thermodynamic equilibrium of the reaction between gas-phase NH_3 and HNO_3 and the content of particle-phase NH_4NO_3 (Fountoukis and Nenes, 2007; Sun et al., 2018). To further explore the influence of RH and T on NO_3^- formation through thermodynamic equilibrium effects, particulate NH_4NO_3 was estimated using the ISORROPIA II model (http://isorropia.eas.gatech.edu/). ISORROPIA II is a thermodynamic equilibrium model for the K^+–Ca^{2+}–Mg^{2+}–NH_4^+–Na^+–SO_4^{2-}–NO_3^- –Cl^-–H_2O aerosol system (Fountoukis and Nenes, 2007). It can be used to analyze gas-, liquid-, and particle-phase steady-state levels of inorganic compounds by iteratively running the reverse mode using ion concentration, RH, and T data. The results showed that the main forms of particulate inorganic ions were Na_2SO_4, NH_4Cl, NH_4NO_3, $(NH4)_2SO_4$, $CaSO_4$, K_2SO_4, and $MgSO_4$. Particle-phase NH_4NO_3 showed notable seasonal variations, with the highest levels in cool seasons and the lowest in warm seasons (Text S6, Fig. S4). During the warm seasons, the deliquescence relative humidity (DRH) of NH_4NO_3 was about 62% due to the high T (25.7 ± 4.0 °C), which was far below the observed RH (75 ± 8%), accelerating the deliquescence of NH_4NO_3. By contrast, the DRH of NH_4NO_3 was approximately 66% at the lower T (21.7 ± 5.3 °C) of the cool seasons, which was higher than the RH (64 ± 11%) and thus did not support the deliquescence of NH_4NO_3, instead favoring the formation of particulate NH_4NO_3 (Fountoukis and Nenes, 2007). This effect, combined with the low and stable boundary layer and relatively strong continental outflow from the central PRD, may increase the particulate NO_3^- concentration and thus the contribution of particulate NO_3^- to the total $PM_{2.5}$ load.

Formation pathway is another factor that may control the seasonal variations of particulate NO_3^-. In this study, O_3 showed no relationship with NO_3^-, whereas N_2O_5 was significantly positively correlated with NO_3^- levels ($R_{N2O5–NO3-} = 0.59$, $P < 0.001$). N_2O_5 concentrations showed an obvious seasonal trend, with higher values during cool seasons (10.8 ± 8.0 pptv) and lower values during warm seasons (1.2 ± 1.3 pptv) (Fig. S4). This result indicates that NO_3^- formed through N_2O_5 hydrolysis is an important cause of high NO_3^- levels during dry and cold seasons in the PRD (Yun et al., 2018).

3.2. Nitrogen isotopes of NO_3^-

During the sampling period, the values of $\delta^{15}N$–NO_3^- varied from −3.60 to 15.4‰ (average: 7.50 ± 3.30‰) (Fig. 1). The results showed seasonal variations, with high levels in fall (8.3 ± 2.6‰) and low values in spring (4.8 ± 3.6‰) (Table S2). These results were consistent with the range of $\delta^{15}N$–NO_3^- measured in precipitation in Guangzhou from 2008 to 2009, where lower values were also observed in spring (Fang et al., 2011). These findings suggest that the nitrogen source distribution of NO_3^- in this region may not have changed markedly over recent years. Spatially, the results were comparable to those from suburban areas of China, where NO_3^- mainly originated from anthropogenic sources, including coal combustion and vehicle exhaust, such as Beihuangcheng Island in northern China (8.20 ± 6.20‰) (Zong et al., 2017), and Dongbeiwang in Beijing (6.80‰) (Zhang et al., 2008), However, our results were markedly higher than those from clean background sites, where NO_3^- was predominately derived from natural sources, including

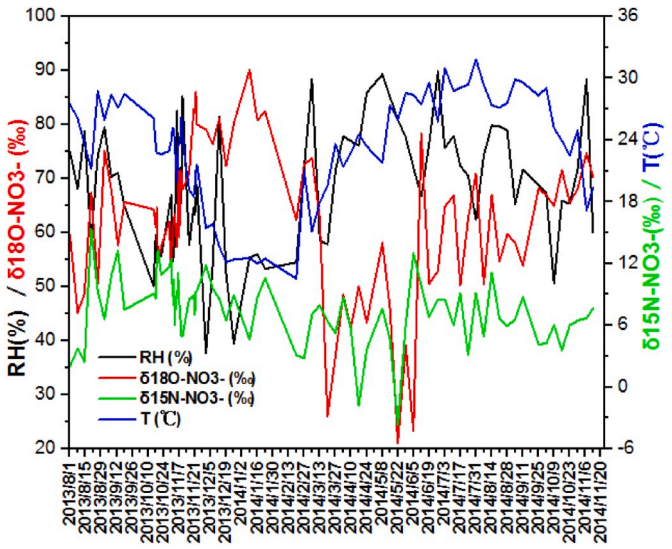

Fig. 1. Temporal variation of $\delta^{15}N$–NO_3^-, $\delta^{18}O$–NO_3^-, the major environmental parameters (RH and T) at HS station during the sampling time.

lightning and biogenic processes, such as Mt. Lulin in central Taiwan (−3.00 ± 3.00‰) (Guha et al., 2017), the Islands of Bermuda (−4.00 ± 0.600‰) (Hastings et al., 2003), and coastal Antarctica (−12.4 ± 7.20‰) (Savarino et al., 2007).

$\delta^{15}N$–NO_3^- was prominently influenced by contributions from multiple NO_x sources (Zong et al., 2017). In the cool seasons, air masses arrived primarily from continental areas with large anthropogenic source contributions, resulting in higher $\delta^{15}N$ values (8.1 ± 2.7‰). However, in the warm seasons, air masses originated mainly from oceanic regions with greater natural source contributions, resulting in lower $\delta^{15}N$ values (6.4 ± 3.9‰). Additionally, $\delta^{15}N$–NO_3^- values were influenced by nitrogen bonding, T-dependent equilibrium fractionation, and changes in reaction pathways (Savard et al., 2017). Studies have indicated that equilibrium isotopic fractionation between NO and NO_2 and between N_2O_5 and NO_2 strongly influence $\delta^{15}N$ values (Hastings et al., 2003; Walters and Michalski, 2015, 2016). Given the larger nitrogen equilibrium fractionation factors ($^{15}\alpha_{NO2/NO} = 1.037$ at 300 K, $^{15}\alpha_{N2O5/NO2} = 1.026$ at 300 K), the partitioning of ^{15}N into NO_2 and N_2O_5, respectively, is favored, which results in higher $\delta^{15}N$ values in NO_3^-. The NO_x/O_3 ratio has been used as a proxy for the equilibrium effect between NO and NO_2, which decreases with strengthening of the equilibrium fractionation effect, while the N_2O_5/NO_2 ratio may represent the effect of equilibrium between N_2O_5 and NO_2, because it increases with a stronger equilibrium effect (Hastings et al., 2003). As shown in Table S4, the elevated NO_x/O_3 ratio (2.96 ± 5.61) and reduced N_2O_5/NO_2 ratio (1.03 ± 0.74) in spring suggested decreases of both fractionation effects, corresponding to the lowest $\delta^{15}N$–NO_3^- value for NO_3^-. The ratio of N_2O_5/NO_2 (3.67 ± 2.06) in cool seasons was significantly higher than that in warm seasons (0.86 ± 0.56), while the NO_x/O_3 ratio in cool seasons (1.42 ± 1.50) was lower than that in spring, indicating that these two equilibrium effects promoted the enrichment of $\delta^{15}N$ in cool seasons. In addition, the ratio of NO_2/NO_x can be used to represent the equilibrium between NO and NO_2 (Fang et al., 2011; Jia and Chen, 2010), and this ratio was higher during the cool seasons (0.89 ± 0.06) than the warm seasons (0.76 ± 0.10). These results indicate that the increased equilibrium effect at low T is one of the main drivers of high $\delta^{15}N$ in cool seasons. These effects, in combination with the continental transport influence noted above, operated synergistically to elevate the $\delta^{15}N$–NO_3^- value in cool seasons. This synergism was particularly strong in fall, when the highest O_3 levels and N_2O_5 levels occur, leading to strengthened fractionation effects compared to winter, and eventually resulting in the highest $\delta^{15}N$–NO_3^- values. The lack of

obvious differences between summer and winter may be attributed to antagonism between changes in reaction pathways and other factors, including equilibrium and transport effects. These two factors led to increased $\delta^{15}N–NO_3^-$ values in winter compared with those in summer. By contrast, higher concentrations of NO_3 and organic compounds in winter favored the formation of NO_3^- through hydrogen abstraction from organic compounds by NO_3 (Text S1, reaction R7), which caused lower $\delta^{15}N$ values and thereby drove the downward trend of $\delta^{15}N–NO_3^-$ values (Walters and Michalski, 2016). Moreover, the change of source emission intensity also affected the abrupt change in $\delta^{15}N–NO_3^-$ values (Savard et al., 2017), as indicated by the significantly higher K^+ levels (biomass burning signal) in winter (0.79 ± 0.48 μg/m^3) compared to spring (0.39 ± 0.32 μg/m^3).

RH and the form of NO_3^- also affected the $\delta^{15}N–NO_3^-$ value. RH was negatively correlated with $\delta^{15}N–NO_3^-$ values in this study ($R_{RH\text{-}NO3\text{-}} = -0.33$, $P < 0.005$), and RH in summer ($RH = 74 \pm 7\%$) was higher than that in winter ($RH = 56 + 13\%$). High RH promotes the homogeneous reaction of ·OH, but hinders the N_2O_5 reaction pathway, resulting in lower $\delta^{15}N$ values in summer (Fang et al., 2011; Walters and Michalski, 2016).

3.3. Oxygen isotopes of NO_3^-

The $\delta^{18}O–NO_3^-$ values varied from 21.0 to 90.1‰ (average: 62.4 ± 14.0‰) (Fig. 1, Table S2). As with the seasonal variations of $\delta^{15}N–NO_3^-$, it was characteristically high in winter and low in spring and summer. The values were comparable to precipitation $\delta^{18}O–NO_3^-$ in Guangzhou (66.3 ± 2.8‰) (Fang et al., 2011), but lower than values in regions at higher latitude, where weak solar intensity may weaken the ·OH reaction pathway of NO_3^- formation, such as Beihuangcheng Island (76.6 ± 8.1‰) (Zong et al., 2017), the Islands of Bermuda (71.1 ± 3.0‰) (Hastings et al., 2003), and coastal Antarctica (80.8 ± 7.2‰) (Savarino et al., 2007).

Oxygen stable isotopic analysis of NO_3^- has frequently been used to assess changes in NO_x oxidation and evaluate long-term trends in the atmosphere's oxidation capacity (Walters and Michalski, 2016). Studies have estimated $\delta^{18}O–NO_3^-$ values corresponding to four different NO_x oxidation pathways in the absence of oxygen isotopic exchange between NO_x and NO_y species, including the N_2O_5 pathway through reactions R4–R6 ($\delta_1 = 102$‰), the ·OH pathway through reactions R1–R3 ($\delta_2 = 55$‰), the $\cdot HO_2+N_2O_5$ pathway through reactions R8–R9 and R4–R6 ($\delta_3 = 28$‰) and the $\cdot HO_2+$·OH pathway through reactions R1–R3 and R8–R9 ($\delta_4 = 11$‰)(Fang et al., 2011; Guha et al., 2017; Walters and Michalski, 2016). Fig. 2 summarizes these $\delta^{18}O–NO_3^-$ values for various pathways, with $\delta^{18}O–NO_3^-$ plotted against $\delta^{15}N–NO_3^-$ and the atmospheric NO_3^- concentration. The samples collected in different seasons were clearly plotted in different areas. The $\delta^{18}O–NO_3^-$ values of most samples, especially those from autumn and winter, were between 55‰ and 102‰, and generally closer to 55‰, indicating that the ·OH pathway was the main pathway of NO_3^- formation in the PRD region. The $\delta^{18}O–NO_3^-$ values of most high-NO_3^- samples collected during the cool seasons ranged from 70‰ to 90‰, supporting the importance of N_2O_5 hydrolysis to NO_3^- formation on hazy days (Yun et al., 2018). Samples with $\delta^{18}O–NO_3^-$ values of less than 55‰ were mainly found in spring and summer, and one sample ($\delta = 21$‰; collected on May 22, 2014) was below 28%. Peroxy radicals ($\cdot HO_2$ and its organic homologues, denoted $\cdot RO_2$) are expected to have $\delta^{18}O$ values much lower than that of O_3, because their oxygen atoms should originate from atmospheric O_2, which can compete with O_3 to convert NO into NO_2 (Fang et al., 2011). Research has determined the rate constants for the conversion of NO into NO_2 by O_3 ($K_{O3} = 1.9 \times 10^{-14}$ cm^3/s) and peroxy radicals ($K_{\cdot HO2} = 8.1 \times 10^{-12}$ cm^3/s) at 298 K, indicating that the peroxy radical reaction is 400 times greater that of O_3 (Sandu and Sander, 2006). However, the atmospheric O_3 level is much higher than that of $\cdot HO_2$. If the $\cdot HO_2$ reaction contributed to the value, we would assume that $K_{\cdot HO2} \times [\cdot HO_2] > K_{O3} \times [O_3]$. O_3 levels in the PRD were moderate,

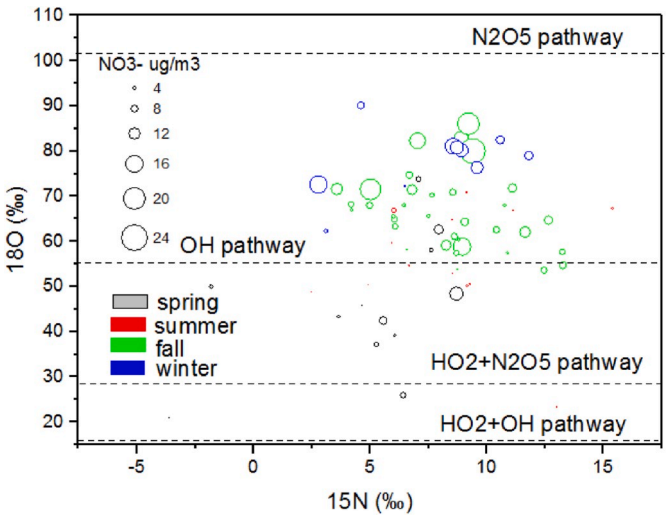

Fig. 2. Plot of $\delta^{15}N–NO_3^-$ vs. $\delta^{18}O–NO_3^-$ at HS station in four seasons. The size of the circles corresponds to the concentration of nitrate aerosol. The dot line shows the O isotopic values in four main pathway.

with O_3 concentrations of 2.2–65.5 ppbv (mean: 27.1 ± 15.0 ppbv). Consequently, we could conclude that the concentration of $\cdot HO_2$ should be greater than 63.6 pptv. A concentration of $\cdot HO_2$ of 67 pptv, measured at noon on a summer day in the PRD, supports the possibility of this conclusion (Hofzumahaus et al., 2009). It has been suggested that the peroxy radical reaction is an important pathway for NO_3^- formation in spring and summer (Fang et al., 2011; Guha et al., 2017). In addition, T and RH influence the seasonal variations of $\delta^{18}O–NO_3^-$ values. Both of these factors were significantly negatively correlated with $\delta^{18}O–NO_3^-$ values ($R_{T\ -\delta18O-NO3-} = -0.44$, $P < 0.001$, $R_{RH\ -\delta18O-NO3-} = -0.34$, $P < 0.001$). This effect is caused by changes in the formation pathway of NO_3^- under different T and RH conditions. For example, the N_2O_5 hydrolysis pathway occurs at low T and RH, leading to high $\delta^{18}O–NO_3^-$ values, whereas the pathway involving ·OH or peroxy radicals, associated with relatively low $\delta^{18}O–NO_3^-$ values, is dominant at high T and RH. Meanwhile, the equilibrium isotope fractionation factors of $\delta^{18}O$ between NO_2 and NO and between ·OH and H_2O are T dependent (Walters and Michalski, 2016). At lower T in winter, the effect of oxygen isotopic exchange between NO_x and oxidation products increases. Equilibrium fractionation will favor the partitioning of ^{18}O into NO_x due to low oxygen equilibrium fractionation factors ($^{18}\alpha_{NO2/NO} = 0.992$ at 300 K, $^{18}\alpha_{NO3/NO2} = 0.9819$ at 300 K), resulting in low $\delta^{18}O–NO_3^-$ values.

Based on the measured $\delta^{18}O–NO_3^-$ values, the gas-phase reaction of NO_2 and ·OH radicals and the hydrolysis of N_2O_5 are the two major pathways of particulate NO_3^- formation in South China, except in a few samples affected by the peroxy radical reaction during the hot and wet season. Excluding samples with $\delta^{18}O–NO_3^-$ values of less than 40‰, a Monte Carlo simulation was performed to illustrate the relative contributions of the ·OH and N_2O_5 pathways to NO_3^- formation during the sampling period. A detailed introduction of the simulation has been reported previously (Zong et al., 2017). As shown in Fig. 3, the median values of the ·OH generation pathway contribution varied seasonally, with higher values in warm seasons and lower values in cool seasons. Specifically, the proportional contributions were 0.72 ± 0.16, 0.76 ± 0.16, 0.63 ± 0.17, and 0.39 ± 0.15 in spring, summer, fall, and winter, respectively, after correcting outliers with ratios higher than 90% based on data from five cities (Zong et al., 2020). The seasonal variations observed in this study were similar to those measured in northern China, but the contribution of the ·OH generation pathway was greater (Zong et al., 2017). To further explore the accuracy of our results about the ·OH generation pathway contribution, the ·OH concentration was estimated using a nonlinear formula, as described in Text S11 (Rohrer, 2000). The

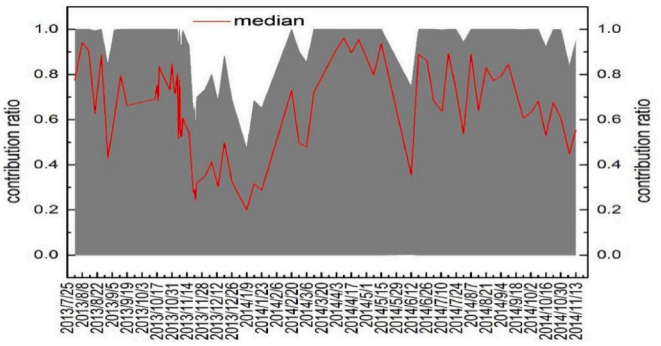

Fig. 3. The range and median of contribution ratio (γ) for the isotopic fractionation through the •OH pathway. The red line is the median of γ and the gray region refers to the range of γ. (For interpretation of the references to colour in this figure legend, the reader is referred to the Web version of this article.)

results showed that the·OH generation pathway contribution had a significant positive correlation with·OH concentration ($P = 0.52$, $r < 0.01$), lending some support to the results of Monte Carlo simulation. Consequently, the ·OH concentrations were 2.5 ± 1.4, 4.8 ± 1,1, 1.5 ± 1.0, and 0.84 ± 0.29 10^6/cm^3 in spring, summer, fall, and winter, respectively.

3.4. Source apportionment of NO_x/NO_3^- using the Bayesian model and PSCF

Based on the results of previous studies conducted in the PRD (Li et al., 2017; Lu et al., 2016), the relationships between NO_3^- and trace species found in $PM_{2.5}$ samples, and auxiliary data including the presence of container terminals and the area of cultivated land in the PRD (Text S8), the predominant sources of NO_x/NO_3^- in the PRD were identified as coal combustion, mobile sources (ship and vehicle emissions), biomass burning, and microbial sources (mainly oceanic). The corresponding $\delta^{15}N$ values of each representative source were input into the improved Bayesian mixing model to apportion the contributions of NO_x/NO_3^- sources (Table S5) (Zong et al., 2017). The average contributions of coal combustion, mobile sources, biomass burning, and microbial sources were 50.1 ± 13.8%, 22.1 ± 4.5%, 18.4 ± 5.1%, and 9.4 ± 4.7%, respectively. These results suggested that coal combustion was the dominant source of NO_3^- in the PRD despite the lack of coal combustion for heating during the cool seasons, followed by biomass burning, mobile sources, and microbial sources. The large contribution of coal combustion might be attributed to power plants, because values comparable to our results (50.0%) were obtained using a comprehensive method based on CAMx and OSAT in a previous study (Lu et al., 2016). Moreover, the contribution of microbial sources found in this study was similar to that (9.65%) obtained from modeling (Lu et al., 2016). However, due to the absence of a contribution from biomass burning in the CAMx and OSAT method (Lu et al., 2016) and the possibility of overlap between $\delta^{15}N$-NO_X signals from biomass burning and mobile sources (Fibiger and Hastings, 2016), the contributions of biomass burning and mobile sources obtained through the two methods were quite different. The results of the MIX inventory showed markedly different proportions compared with the results of this study (Li et al., 2017). It has been reported that 30% of power and industrial fuels are from biomass sources in the PRD (Li et al., 2017). Thus, the relative contributions of coal combustion and biomass burning would be 48.6% and 20.85%, respectively, based on the MIX inventory method under the assumption that 30% of fuel arises from biomass. However, the large contribution from mobile sources (28.2%) and small contribution from marine sources (zero) obtained from the MIX inventory were due to the absence of the marine source from that method.

Fig. 4 shows the seasonal NO_3^- contributions of four main sources in the PRD. The ranges and median values of the sources were similar in winter and summer. However, the range and median of coal combustion in fall (40.3–60.2% and 50%) increased significantly compared with those in spring (31.6–49.5% and 40%). In fall, the large contribution from coal combustion was attributed to the continental origin of the air mass, which crossed most of the economically developed areas of the PRD (Fig. S10). This result was supported by the strong correlations of coal combustion signals (EC, nss-Cl^-, SO_4^{2-}, and NH_4^+) with NO_3^- in fall (Fig. S9). In spring, air masses were mainly of oceanic origin (SCS and MP) and showed relative high contributions from mobile sources, oceanic sources and biomass burning compared with that in fall, resulting in a smaller contribution from coal combustion. This result was verified by the concentration of coal combustion signals (EC, nss-SO_4^{2-}, NH_4^+, and nss-Cl^-) from FJ and JX being significantly higher than those from SCS and MP (Fig. S8).

Due to the significant influence of regional sources and transport of NO_3^- on nitrogen pollution in the PRD, PSCF was employed to identify the potential source regions of the four main NO_3^- sources obtained from the improved Bayesian model. A detailed description of the PSCF method and its results can be found in Text S5 and Fig. S10. In summary, the coal combustion source was mainly located in the central and eastern PRD, biomass burning mainly arose from the northeast area of Guangdong Province, and mobile and microbial sources did not show any obvious regional pattern. Considering the dominant contributions of coal combustion and biomass burning to NO_3^-, relevant source control policies must be implemented regionally and provincially to reduce NO_3^- pollution and improve public health.

4. Conclusions

In this study, NO_3^- concentrations ranged from 0.60 to 21.7 μg/m^3 (average: 5.40 ± 4.80 μg/m^3), and accounted for 1–16% of $PM_{2.5}$ masses in the PRD. Obvious seasonal trends of NO_3^- were observed with the highest values in fall and the lowest in summer. The seasonal concentrations of particulate NO_3^- were mainly controlled by air mass transport pattern, potential sources, meteorological parameters, and NO_3^- formation pathway. During the sampling period, the values of $\delta^{15}N$– NO_3^- varied from −3.60 to 15.4‰ (average: 7.50 ± 3.30‰). It showed clearly seasonal variation characteristics of high in fall and low in spring. Besides influenced by the different NO_x sources, the values of $\delta^{15}N$– NO_3^- were also affected by the equilibrium fractionation effects of NO_3^- formation with the different meteorological parameters. The $\delta^{18}O$–NO_3^-values varied from 21.0 to 90.1‰ (average: 62.4 ± 14.0‰). In spring, the lowest $\delta^{18}O$– NO_3^- values were observed due to high

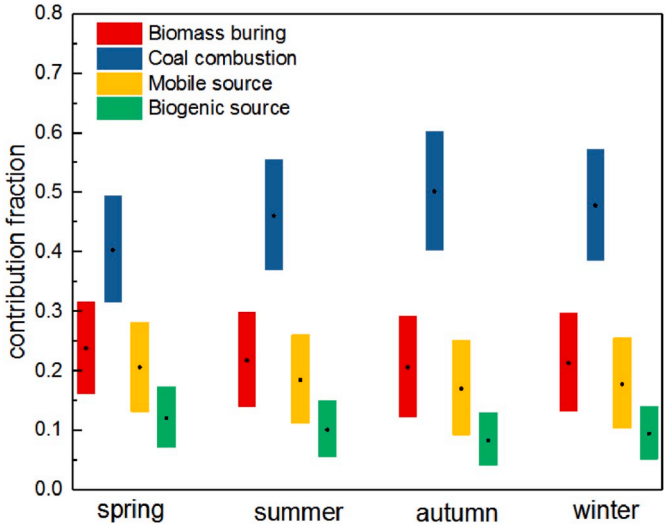

Fig. 4. Contribution fraction of NO_x/NO_3^- source in different seasons, including the range from the first to third quartiles and the median value.

proportions from the $\cdot HO_2$ reaction and the ·OH pathway. In winter, the highest $\delta^{18}O$– NO_3^- values were observed due to cold and dry weather and the lowest proportion from the ·OH pathway. Based on the measured $\delta^{18}O$– NO_3^- values, the relative contributions from gas-phase reaction between NO_2 and ·OH radicals and the hydrolysis of N_2O_5 were estimated by a Monte Carlo simulation. Consequently, ·OH generation pathway was the predominant pathway, and the proportional contributions were 0.72 ± 0.18, 0.76 ± 0.16, 0.63 ± 0.17 and 0.39 ± 0.15 in spring, summer, fall and winter, respectively. The potential sources of NO_x/NO_3^- were apportioned by the improved Bayesian mixing model. Results showed the average contributions of coal combustion, mobile source, biomass burning and microbial source were 50.1 ± 13.8%, 22.1 ± 4.5%, 18.4 ± 5.1% and 9.4 ± 4.7%, respectively. PSCF results showed the sources of coal combustion arose from the central and southern in Guangdong Province and the surrounding areas in the northeast.

Declaration of competing interest

The authors declare that they have no known competing financial interests or personal relationships that could have appeared to influence the work reported in this paper.

CRediT authorship contribution statement

Tao Su: Writing - original draft, Validation, Data curation. **Jun Li:** Conceptualization, Supervision, Writing - review & editing. **Chongguo Tian:** Data curation, Methodology, Writing - review & editing. **Zheng Zong:** Methodology, Data curation, Methodology. **Duohong Chen:** Conceptualization, Supervision. **Gan Zhang:** Conceptualization, Writing - review & editing.

Acknowledgment

This work is funded by the Natural Science Foundation of China (NSFC; nos. 41977177), the National Key R&D Program of China (2017YFC0212000) and Guangdong Foundation for Program of Science and Technology Research (Grant No. 2017B030314057). This is contribution NO. IS-2859 from GIGCAS.

Appendix A. Supplementary data

Supplementary data to this article can be found online at https://doi.org/10.1016/j.atmosenv.2020.117563.

References

Brown, S.S., Osthoff, H.D., Stark, H., Dubé, W.P., Ryerson, T.B., Warneke, C., de Gouw, J. A., Wollny, A.G., Parrish, D.D., Fehsenfeld, F.C., Ravishankara, A.R., 2005. Aircraft observations of daytime NO3 and N2O5 and their implications for tropospheric chemistry. J. Photochem. Photobiol. Chem. 176, 270–278.
Cao, J., 2014. PM2.5 and Environment in China. Science press, Beijing.
Cao, J.J., Shen, Z.X., Chow, J.C., Watson, J.G., Lee, S.C., Tie, X.X., Ho, K.F., Wang, G.H., Han, Y.M., 2012. Winter and summer PM2.5 chemical compositions in fourteen Chinese cities. J. Air Waste Manag. Assoc. 62, 1214–1226.
Cheng, M.-D., Kabela, E.D., 2016. Effects of downscaled high-resolution meteorological data on the PSCF identification of emission sources. Atmos. Environ. 137, 146–154.
Fang, Y.T., Koba, K., Wang, X.M., Wen, D.Z., Li, J., Takebayashi, Y., Liu, X.Y., Yoh, M., 2011. Anthropogenic imprints on nitrogen and oxygen isotopic composition of precipitation nitrate in a nitrogen-polluted city in southern China. Atmos. Chem. Phys. 11, 1313–1325.
Felix, J.D., Elliott, E.M., 2014. Isotopic composition of passively collected nitrogen dioxide emissions: vehicle, soil and livestock source signatures. Atmos. Environ. 92, 359–366.
Fibiger, D.L., Hastings, M.G., 2016. First measurements of the nitrogen isotopic composition of NOx from biomass burning. Environ. Sci. Technol. 50, 11569–11574.
Fountoukis, C., Nenes, A., 2007. ISORROPIA II: a computationally efficient thermodynamic equilibrium model for K+-Ca2+-Mg2+-Nh(4)(+)-Na+-SO42NO3ClH2O aerosols. Atmos. Chem. Phys. 4639–4659.
Guha, T., Lin, C.T., Bhattacharya, S.K., Mahajan, A.S., Ou-Yang, C.F., Lan, Y.P., Hsu, S.C., Liang, M.C., 2017. Isotopic ratios of nitrate in aerosol samples from Mt. Lulin, a high-altitude station in Central Taiwan. Atmos. Environ. 154, 53–69.
Han, K.M., Song, C.H., Ahn, H.J., Park, R.S., Woo, J.H., Lee, C.K., Richter, A., Burrows, J. P., Kim, J.Y., Hong, J.H., 2009. Investigation of NOx emissions and NOx- related chemistry in East Asia using CMAQ-predicted and GOME-derived NO2 columns. Atmos. Chem. Phys. 9, 1017–1036.
Hastings, M.G., Sigman, D.M., Lipschultz, F., 2003. Isotopic evidence for source changes of nitrate in rain at Bermuda. J. Geophys. Res. Atmos. 108.
Hofzumahaus, A., Rohrer, F., Lu, K., Bohn, B., Brauers, T., Chang, C.-C., Fuchs, H., Holland, F., Kita, K., Kondo, Y., Li, X., Lou, S., Shao, M., Zeng, L., Wahner, A., Zhang, Y., 2009. Amplified trace gas removal in the troposphere. Science 324, 1702–1704.
Jia, G., Chen, F., 2010. Monthly variations in nitrogen isotopes of ammonium and nitrate in wet deposition at Guangzhou, south China. Atmos. Environ. 44, 2309–2315.
Komatsu, D.D., Ishimura, T., Nakagawa, F., Tsunogai, U., 2008. Determination of the 15N/14N, 17O/16O, and 18O/16O ratios of nitrous oxide by using continuous-flow isotope-ratio mass spectrometry. Rapid Commun. Mass Spectrom. : RCM (Rapid Commun. Mass Spectrom.) 22, 1587–1596.
Li, J., Zhang, G., Li, X.D., Qi, S.H., Liu, G.Q., Peng, X.Z., 2006. Source seasonality of polycyclic aromatic hydrocarbons (PAHs) in a subtropical city, Guangzhou, South China. Sci. Total Environ. 355, 145–155.
Li, M., Zhang, Q., Kurokawa, J., Woo, J.H., He, K.B., Lu, Z.F., Ohara, T., Song, Y., Streets, D.G., Carmichael, G.R., Cheng, Y.F., Hong, C.P., Huo, H., Jiang, X.J., Kang, S. C., Liu, F., Su, H., Zheng, B., 2017. MIX: a mosaic Asian anthropogenic emission inventory under the international collaboration framework of the MICS-Asia and HTAP. Atmos. Chem. Phys. 17, 935–963.
Liu, J., Li, J., Zhang, Y., Liu, D., Ding, P., Shen, C., Shen, K., He, Q., Ding, X., Wang, X., Chen, D., Szidat, S., Zhang, G., 2014. Source apportionment using radiocarbon and organic tracers for PM2.5 carbonaceous aerosols in Guangzhou, South China: contrasting local- and regional-scale haze events. Environ. Sci. Technol. 48, 12002–12011.
Lu, K.D., Rohrer, F., Holland, F., Fuchs, H., Brauers, T., Oebel, A., Dlugi, R., Hu, M., Li, X., Lou, S.R., Shao, M., Zhu, T., Wahner, A., Zhang, Y.H., Hofzumahaus, A., 2014. Nighttime observation and chemistry of HOx in the Pearl River delta and Beijing in summer 2006. Atmos. Chem. Phys. 14, 4979–4999.
Lu, X.C., Fung, J.C.H., 2016. Source apportionment of sulfate and nitrate over the Pearl River delta region in China. Atmosphere 7, 13.
Lu, X.C., Yao, T., Li, Y., Fung, J.C.H., Lau, A.K.H., 2016. Source apportionment and health effect of NOx over the Pearl River Delta region in southern China. Environ. Pollut. 212, 135–146.
Ma, Y.F., Lu, K.D., Chou, C.C.K., Li, X.Q., Zhang, Y.H., 2017. Strong deviations from the NO-NO2-O-3 photostationary state in the Pearl River Delta: indications of active peroxy radical and chlorine radical chemistry. Atmos. Environ. 163, 22–34.
McIlvin, M.R., Altabet, M.A., 2005. Chemical conversion of nitrate and nitrite to nitrous oxide for nitrogen and oxygen isotopic analysis in freshwater and seawater. Anal. Chem. 77, 5589–5595.
Ming, L., Jin, L., Li, J., Fu, P., Yang, W., Liu, D., Zhang, G., Wang, Z., Li, X., 2017. PM2.5 in the Yangtze River Delta, China: chemical compositions, seasonal variations, and regional pollution events. Environ. Pollut. 223, 200–212.
Moore, J.W., Semmens, B.X., 2008. Incorporating uncertainty and prior information into stable isotope mixing models. Ecol. Lett. 11, 470–480.
Rohrer, D.H.E.a.F., 2000. Dependence of the OH concentration on solar UV. J. Geophys. Res. 16, 3565–3571.
Sandu, A., Sander, R., 2006. Technical note: simulating chemical systems in Fortran90 and Matlab with the kinetic PreProcessor KPP-2.1. Atmos. Chem. Phys. 6, 187–195.
Savard, M.M., Cole, A., Smirnoff, A., Vet, R., 2017. Delta N-15 values of atmospheric N species simultaneously collected using sector - based samplers distant from sources Isotopic inheritance and fractionation. Atmos. Environ. 162, 11–22.
Savarino, J., Kaiser, J., Morin, S., Sigman, D.M., Thiemens, M.H., 2007. Nitrogen and oxygen isotopic constraints on the origin of atmospheric nitrate in coastal Antarctica. Atmos. Chem. Phys. 7, 1925–1945.
Sheehan, P., Cheng, E., English, A., Sun, F., 2014. China's response to the air pollution shock. Nat. Clim. Change 4, 306–309.
Shimadera, H., Kojima, T., Kondo, A., Inoue, Y., 2015. Performance comparison of CMAQ and CAMx for one-year PM2.5 simulation in Japan. Int. J. Environ. Pollut. 57, 146–161.
Sun, P., Nie, W., Chi, X., Xie, Y., Huang, X., Xu, Z., Qi, X., Xu, Z., Wang, L., Wang, T., Zhang, Q., Ding, A., 2018. Two years of online measurement of fine particulate nitrate in the western Yangtze River Delta: influences of thermodynamics and N2O5 hydrolysis. Atmos. Chem. Phys. 18, 17177–17190.
Tao, J., Zhang, L.M., Cao, J.J., Zhang, R.J., 2017. A review of current knowledge concerning PM2.5 chemical composition, aerosol optical properties and their relationships across China. Atmos. Chem. Phys. 17, 9485–9518.
Tao, J., Zhang, Z., Tan, H., Zhang, L., Wu, Y., Sun, J., Che, H., Cao, J., Cheng, P., Chen, L., Zhang, R., 2018. Observational evidence of cloud processes contributing to daytime elevated nitrate in an urban atmosphere. Atmos. Environ. 186, 209–215.
Walters, W.W., Michalski, G., 2015. Theoretical calculation of nitrogen isotope equilibrium exchange fractionation factors for various NOy molecules. Geochem. Cosmochim. Acta 164, 284–297.
Walters, W.W., Michalski, G., 2016. Theoretical calculation of oxygen equilibrium isotope fractionation factors involving various NOy molecules, (OH)-O-center dot, and H2O and its implications for isotope variations in atmospheric nitrate. Geochem. Cosmochim. Acta 191, 89–101.
Xiao, H.-W., Xie, L.-H., Long, A.-M., Ye, F., Pan, Y.-P., Li, D.-N., Long, Z.-H., Chen, L., Xiao, H.-Y., Liu, C.-Q., 2015. Use of isotopic compositions of nitrate in TSP to identify sources and chemistry in South China Sea. Atmos. Environ. 109, 70–78.

Yun, H., Wang, W., Wang, T., Xia, M., Yu, C., Wang, Z., Poon, S.C.N., Yue, D., Zhou, Y., 2018. Nitrate formation from heterogeneous uptake of dinitrogen pentoxide during a severe winter haze in southern China. Atmos. Chem. Phys. 18, 17515–17527.

Zhang, L., Dao, X., Wang, C., Jin, X., Teng, E., Lyu, Y., 2015. Characterization of air particulate matters and elements in four national background locations, China. Environ. Chem. 34, 70–76.

Zhang, Y., Liu, X.J., Fangmeier, A., Goulding, K.T.W., Zhang, F.S., 2008. Nitrogen inputs and isotopes in precipitation in the North China Plain. Atmos. Environ. 42, 1436–1448.

Zhao, B., Wang, S.X., Liu, H., Xu, J.Y., Fu, K., Klimont, Z., Hao, J.M., He, K.B., Cofala, J., Amann, M., 2013. NOx emissions in China: historical trends and future perspectives. Atmos. Chem. Phys. 13, 9869–9897.

Zong, Z., Tan, Y., Wang, X., Tian, C., Li, J., Fang, Y., Chen, Y., Cui, S., Zhang, G., 2020. Dual-modelling-based source apportionment of NOx in five Chinese megacities: providing the isotopic footprint from 2013 to 2014. Environ. Int. 137, 105592-105592.

Zong, Z., Wang, X., Tian, C., Chen, Y., Fu, S., Qu, L., Ji, L., Li, J., Zhang, G., 2018. PMF and PSCF based source apportionment of PM 2.5 at a regional background site in North China. Atmos. Res. 203, 207–215.

Zong, Z., Wang, X.P., Tian, C.G., Chen, Y.J., Fang, Y.T., Zhang, F., Li, C., Sun, J.Z., Li, J., Zhang, G., 2017. First assessment of NOx sources at a regional background site in north China using isotopic analysis linked with modeling. Environ. Sci. Technol. 51, 5923–5931.